

An embedded-atom potential for the Cu–Ag system

P L Williams¹, Y Mishin¹ and J C Hamilton²

¹ School of Computational Sciences, George Mason University, MSN 5C3, 4400 University Drive, Fairfax, VA 22030-4444, USA

² Sandia National Laboratories, Livermore, CA 94551, USA

Received 8 December 2005, in final form 10 April 2006

Published 30 May 2006

Online at stacks.iop.org/MSMSE/14/817

Abstract

A new embedded-atom method (EAM) potential has been constructed for Ag by fitting to experimental and first-principles data. The potential accurately reproduces the lattice parameter, cohesive energy, elastic constants, phonon frequencies, thermal expansion, lattice-defect energies, as well as energies of alternate structures of Ag. Combining this potential with an existing EAM potential for Cu, a binary potential set for the Cu–Ag system has been constructed by fitting the cross-interaction function to first-principles energies of imaginary Cu–Ag compounds. Although properties used in the fit refer to the 0 K temperature (except for thermal expansion factors of pure Cu and Ag) and do not include liquid configurations, the potentials demonstrate good transferability to high-temperature properties. In particular, the entire Cu–Ag phase diagram calculated with the new potentials in conjunction with Monte Carlo simulations is in satisfactory agreement with experiment. This agreement suggests that EAM potentials accurately fit to 0 K properties can be capable of correctly predicting simple phase diagrams. Possible applications of the new potential set are outlined.

1. Introduction

Embedded-atom method (EAM) potentials represent the most common model of atomic bonding in metallic systems [1, 2]. They have been applied to atomistic simulations of point defects, diffusion, plastic deformation, fracture and many other properties. One area where the capabilities of EAM potentials have not yet been well established is the calculation of phase diagrams. Indeed, EAM potentials are usually constructed by fitting to experimental and/or first-principles data for a material at zero degrees Kelvin. It is not evident *a priori* that a potential fit to 0 K properties will be transferable to high temperatures or that it will be capable of reproducing the entire phase diagram of the system.

The ability of EAM potentials to reproduce phase diagrams is very important for many applications of atomistic simulations, including surface and interface segregation, surface wetting, alloy crystallization, phase transformations and interdiffusion. It should be noted that

EAM potentials in conjunction with molecular dynamics and/or Monte Carlo simulations allow thermodynamic calculations beyond the approximations of the lattice-based models, such as cluster-expansion methods. Besides all atomic relaxations, such calculations automatically include atomic vibrations beyond the harmonic approximation and are applicable to both solid and liquid phases. Essentially, the accuracy of EAM-based thermodynamic calculations depends primarily on the accuracy and transferability of the EAM potential.

There have been several phase diagram calculations employing EAM potentials, see for example [3–6] and references therein. Unfortunately, some features of the calculated phase diagrams disagree with experiment even on a qualitative level. For example, the Fe–Cu diagram computed in [5] contains BCC Cu and a continuous BCC solid solution region extending from pure Fe to pure Cu. Hoyt *et al* [4] calculated the high-temperature part of the Cu–Pb phase diagram and achieved a semi-quantitative agreement with experiment, but their interatomic potential had been deliberately fit to reproduce the experimental heats of mixing of liquid alloys. The γ/γ' and γ'/β lines of the Ni–Al phase diagram calculated with an EAM potential [7] were found to be in good agreement with experiment. However, the Ni_5Al_3 phase existing on the experimental diagram at relatively low temperatures was not reproduced by the calculations. The liquidus lines of the Ni–Al diagram were not computed in [7].

The present work continues the exploration of capabilities of EAM potentials by posing and addressing the following question: given a binary system with a very simple phase diagram, can an EAM potential whose cross-interactions were fit exclusively to first-principles data at 0 K correctly reproduce the entire phase diagram? As a model we choose the Cu–Ag system exhibiting a single eutectic point and containing a Cu-rich FCC solid solution α , an Ag-rich FCC solid solution β and a liquid solution [8,9]. Being very simple, this system still contains such basic features as a miscibility gap, solid–solid and solid–liquid equilibria that need to be reproduced by the potential correctly. The next level of complexity would be a diagram with an intermediate phase, which could be the subject of our future work.

All EAM potentials for the Cu–Ag system known to us (e.g. [10–12]) have been constructed by fitting to experimental data only, with the cross-interaction function fit to experimental heats of formation of dilute solid solutions. Using Monte Carlo simulations and thermodynamic integration with the Foiles, Baskes and Daw (FBD) potential [10], Webb *et al* [13] calculated the high-temperature part of the Cu–Ag phase diagram and obtained a rough estimate of the eutectic point by linear extrapolation of the liquidus lines. However, the solvus lines were not calculated in [13] (this had been done in a separate paper [14] using the same FBD potential but a different thermodynamic model). On the other hand, Najafabadi *et al* [15] computed the solvus lines using the FBD potential in conjunction with a free-energy minimization technique based on the mean-field approximation to the configurational entropy and the local harmonic approximation to atomic vibrations. All these authors found reasonable agreement with the relevant parts of the experimental phase diagram. For the solvus lines this is not very surprising given that the potential was fit to experimental solution heats, but the agreement observed for the liquidus lines is encouraging since liquid properties were not included in the fit.

In this paper we reconstruct the entire Cu–Ag phase diagram using a new EAM potential set developed in this work. While the pure Cu and pure Ag potentials were developed by fitting to both experimental and first-principles data, the cross-interaction potential is only fit to first-principles energies of imaginary Cu–Ag compounds at 0 K. No liquid properties, experimental or first-principles, are used in the potential construction. Moreover, except for thermal expansion factors of pure Cu and Ag, all target properties used in the potential fit refer to 0 K. This deliberately chosen strategy is designed to evaluate the transferability of the potential to high-temperature properties, including liquid phases.

2. Embedded-atom potential for the Cu–Ag system

The EAM represents the total energy of an atomic system in the form [1]

$$E_{\text{tot}} = \frac{1}{2} \sum_{ij} V_{ij}(r_{ij}) + \sum_i F_i(\bar{\rho}_i). \quad (1)$$

Here $V_{ij}(r_{ij})$ is the pair interaction energy between atoms i and j separated by a distance r_{ij} and F_i is the embedding energy of atom i as a function of the host electron density $\bar{\rho}_i$. The latter is given by

$$\bar{\rho}_i = \sum_{j \neq i} \rho_j(r_{ij}), \quad (2)$$

where $\rho_j(r)$ is the electron density function assigned to atom j . An EAM description of an elemental system requires three functions: for example, $V_{\text{AgAg}}(r)$, $\rho_{\text{Ag}}(r)$ and $F_{\text{Ag}}(\bar{\rho})$ for pure Ag. For the binary Cu–Ag system studied here, seven potential functions are required: $V_{\text{CuCu}}(r)$, $V_{\text{CuAg}}(r)$, $V_{\text{AgAg}}(r)$, $\rho_{\text{Cu}}(r)$, $\rho_{\text{Ag}}(r)$, $F_{\text{Cu}}(\bar{\rho})$ and $F_{\text{Ag}}(\bar{\rho})$. The traditional way to construct these functions is to utilize existing potentials for pure Cu and Ag and only fit the cross-interaction potential $V_{\text{CuAg}}(r)$. The invariant transformation parameters [2, 16–18] are also used in this process as adjustable parameters. In this work we construct a Cu–Ag potential set by the following scheme:

- Use an existing EAM potential for Cu constructed in [19].
- Develop a new EAM potential for pure Ag by fitting to experimental and first-principles data.
- Construct the cross-interaction function $V_{\text{CuAg}}(r)$ by fitting to first-principles data only.

2.1. Embedded-atom potential for Ag

Since the parametrization and fitting procedures applied for constructing the Ag potential are very similar to those used previously for Cu [19], only a brief description will be given. The potential is generated directly in the effective pair format [17]. Omitting the chemical subscript ‘Ag’, the pair interaction function $V(r)$ is represented by a superposition of two Morse functions,

$$V(r) = V_M(r) \equiv [E_1 M(r, r_0^{(1)}, \alpha_1) + E_2 M(r, r_0^{(2)}, \alpha_2) + \delta] \psi \left(\frac{r - r_c}{h} \right), \quad (3)$$

if $r \geq r_s^{(1)}$ and

$$V(r) = V_M(r_s^{(1)}) + V'_M(r_s^{(1)})(r - r_s^{(1)}) + \frac{1}{2} V''_M(r_s^{(1)})(r - r_s^{(1)})^2 + \frac{1}{6} V'''_M(r_s^{(1)})(r - r_s^{(1)})^3 + \sum_{n=1}^5 S_n H(r_s^{(n)} - r)(r_s^{(n)} - r)^4 \quad (4)$$

if $r < r_s^{(1)}$. Here,

$$M(r, r_0, \alpha) = \exp(-2\alpha(r - r_0)) - 2 \exp(-\alpha(r - r_0)) \quad (5)$$

is a Morse function, $H(x)$ is a unit step function and $\psi(x)$ is a cutoff function defined as $\psi(x) = 0$ if $x \geq 0$ and $\psi(x) = x^4/(1 + x^4)$ if $x < 0$. Equations (3) and (4) contain the fitting parameters E_1 , E_2 , $r_0^{(1)}$, $r_0^{(2)}$, α_1 , α_2 , δ , r_c , h and $\{r_s^{(n)}, S_n\}_{n=1, \dots, 5}$. The electron density function is parametrized in the form

$$\rho(r) = \rho_d(r) \equiv [A \exp(-\beta_1(r - r_0^{(3)})^2) + \exp(-\beta_2(r - r_0^{(4)}))] \psi \left(\frac{r - r_c}{h} \right) \quad (6)$$

if $r \geq r_d^{(1)}$ and

$$\begin{aligned} \rho(r) = & \rho_d(r_d^{(1)}) + \rho'_d(r_d^{(1)})(r - r_d^{(1)}) + \frac{1}{2}\rho''_d(r_d^{(1)})(r - r_d^{(1)})^2 + \frac{1}{6}\rho'''_d(r_d^{(1)})(r - r_d^{(1)})^3 \\ & + Q_1 \frac{(r - r_d^{(1)})^4}{1 + 9(r - r_d^{(1)})^2} + Q_2 H(r_d^{(2)} - r)(r - r_d^{(2)})^4 \end{aligned}$$

if $r < r_d^{(1)}$, with parameters A , $r_0^{(3)}$, $r_0^{(4)}$, β_1 , β_2 , $r_d^{(1)}$, $r_d^{(2)}$, Q_1 and Q_2 . The cutoff function $\psi(x)$ guarantees that both functions $V(r)$ and $\rho(r)$ as well as their derivatives up to the second one turn smoothly to zero at the cutoff distance r_c .

Two of the above parameters, A and E_1 , are eliminated by normalizing $\rho(r)$ to $\bar{\rho} = 1$ at lattice parameter $a = a_0$ and using the equilibrium condition of the FCC structure with respect to volume variations at the experimental lattice parameter a_0 . This reduces the number of fitting parameters by two.

The embedding function is represented by a polynomial

$$F_p(\bar{\rho}) = F^{(0)} + \frac{1}{2}F^{(2)}(\bar{\rho} - 1)^2 + \sum_{n=1}^4 q_n(\bar{\rho} - 1)^{n+2} \quad (7)$$

if $\bar{\rho} < \bar{\rho}_1$ and

$$F(\bar{\rho}) = F_p(\bar{\rho}_1) + F'_p(\bar{\rho}_1)(\bar{\rho} - \bar{\rho}_1) + \frac{1}{2}F''_p(\bar{\rho}_1)(\bar{\rho} - \bar{\rho}_1)^2 + \frac{1}{6}F'''_p(\bar{\rho}_1)(\bar{\rho} - \bar{\rho}_1)^3 \quad (8)$$

if $\bar{\rho} > \bar{\rho}_1 > 1$. The coefficients $F^{(0)}$ and $F^{(2)}$ can be expressed in terms of the experimental values of the cohesive energy E_0 [20] and the bulk modulus B [21] and are thus eliminated from the list of fitting parameters, while q_1 is determined from the boundary condition $F_p(0) = 0$. Thus, only $\bar{\rho}_1$ and the coefficients q_2 , q_3 , and q_4 are used as fitting parameters for $F(\bar{\rho})$.

Formally, this parametrization of the potential functions includes 30 adjustable parameters. However, only 15 of them are actually used for fitting to physical properties of Ag. The parameters $\bar{\rho}_1$, $r_s^{(n)}$ and S_n are chosen almost arbitrarily so as to make the repulsive part of the binding curve of FCC Ag smooth and somewhat steeper than is predicted by the universal equation of state by Rose *et al* [22]. Likewise, $r_d^{(n)}$ and Q_n are chosen so as to prevent negative values of $\rho(r)$ that could otherwise arise at short atomic separations. Note that this parametrization scheme automatically guarantees an exact fit to a_0 , E_0 and B .

The potential was optimized by minimizing the weighted mean squared deviation of selected properties of Ag from their target values. The experimental part of the fitting database included, besides a_0 , E_0 and B , the elastic constants c_{ij} , the relaxed vacancy formation (E_v^f) and migration (E_v^m) energies, the phonon frequencies at the zone-boundary point X and the intrinsic stacking fault energy γ_{SF} . The thermal expansion factor of FCC Ag at 1000 K was also included with a small weight. The first-principles part of the database contained the energies E (per atom) of the FCC, HCP (with the ideal c/a ratio), BCC, simple cubic (SC) and diamond cubic (DC) structures as functions of the atomic volume Ω . They had been generated with the Vienna *ab initio* simulation package (VASP) [23] within the local density approximation (LDA). Considering that the reference energies of the EAM and VASP calculations are different, the goal was to match the energy differences $E(\Omega) - E_0$ calculated by both methods. Furthermore, before the fitting process all interatomic distances involved in the VASP-generated $E(\Omega)$ functions were scaled by a factor $S = a_0/a_0^{\text{VASP}}$, where $a_0^{\text{VASP}} = 4.020 \text{ \AA}$ is the FCC-equilibrium lattice parameter obtained by VASP calculations. The intention of this scaling is to compensate for the underestimation of interatomic distances inherent in LDA calculations.

Table 1. Optimized values of fitting parameters of the EAM potential for Ag.

Parameter	Value	Parameter	Value
r_c (Å)	5.995 01	β_1 (Å ⁻²)	$1.423\,25 \times 10^{-2}$
h (Å)	0.547 388	β_2 (Å ⁻¹)	$5.763\,23 \times 10^2$
E_2 (eV)	$3.569\,66 \times 10^{-3}$	S_1 (eV Å ⁻⁴)	32.0
$r_0^{(1)}$ (Å)	-7.157 62	S_2 (eV Å ⁻⁴)	-40.0
$r_0^{(2)}$ (Å)	5.284 64	S_3 (eV Å ⁻⁴)	10.0
$r_0^{(3)}$ (Å)	-60.132 24	S_4 (eV Å ⁻⁴)	29.0
$r_0^{(4)}$ (Å)	$-2.614\,31 \times 10^2$	S_5 (eV Å ⁻⁴)	50.0
α_1 (Å ⁻¹)	2.967 60	$r_d^{(1)}$ (Å)	2.5
α_2 (Å ⁻¹)	1.500 08	$r_d^{(2)}$ (Å)	2.0
δ (Å)	$6.568\,90 \times 10^{-4}$	$\bar{\rho}_1$	1.4
$r_s^{(1)}$ (Å)	2.84	q_2 (eV)	$-7.194\,74 \times 10^{-2}$
$r_s^{(2)}$ (Å)	2.80	q_3 (eV)	-0.203 959
$r_s^{(3)}$ (Å)	2.65	q_4 (eV)	0.558 648
$r_s^{(4)}$ (Å)	0.66	Q_1	-5.0
$r_s^{(5)}$ (Å)	0.55	Q_2	-0.1

The optimized values of the fitting parameters are listed in table 1 and the potential functions are shown in figure 1. Tabulated forms of these functions are available from the authors by request.

2.2. Testing of the Ag potential

Table 2 compares lattice properties of Ag calculated with the EAM potential to experimental data [20, 21, 24, 25]. Figure 2 shows that the potential provides good agreement with experimental phonon dispersion curves [25], though some deviations are observed in the high-frequency range (>5 THz).

Thermal expansion factors of FCC Ag were computed by a Monte Carlo method in which atoms in a 864-atom cubic supercell were allowed to move around their lattice positions while the volume could fluctuate to ensure a zero-pressure condition (NPT ensemble) [26, 27]. The agreement with experiment [28] is very good (figure 3). The melting temperature T_m was computed by NPT Monte Carlo simulations using a 3920-atom supercell containing a solid–liquid interface. By observing the direction of the interface motion at various simulation temperatures, T_m could be located with an accuracy of ± 5 K. The value obtained with this potential, $T_m = 1267$ K, is in reasonable agreement with the experimental value 1235 K [20].

Lattice defect energies in Ag calculated with the EAM potential are compared with experimental data in table 3. All defect energies were obtained by fully relaxed calculations. The vacancy formation and migration energies and the intrinsic stacking fault energy were included in the fit, but all other properties are predictions of the potential. The ground state of a self-interstitial is found to be a $\langle 100 \rangle$ -oriented split dumbbell configuration. The interstitial migration energy compares well with experiment. The interstitial dumbbell migrates by a 90° rotation with a simultaneous displacement of its centre of mass by $1/2\langle 110 \rangle$. The unstable stacking fault energy predicted by the potential, $\gamma_{us} = 115$ mJ m⁻², lies between the first-principles result, 190 mJ m⁻² [29], and tight-binding calculations, 95 mJ m⁻² [30]. The surface relaxations calculated for the (100), (110) and (111) orientations (table 4) also agree reasonably well with experimental data and with first-principles calculations. The surface energies underestimate experimental and especially first-principles values, which is the usual

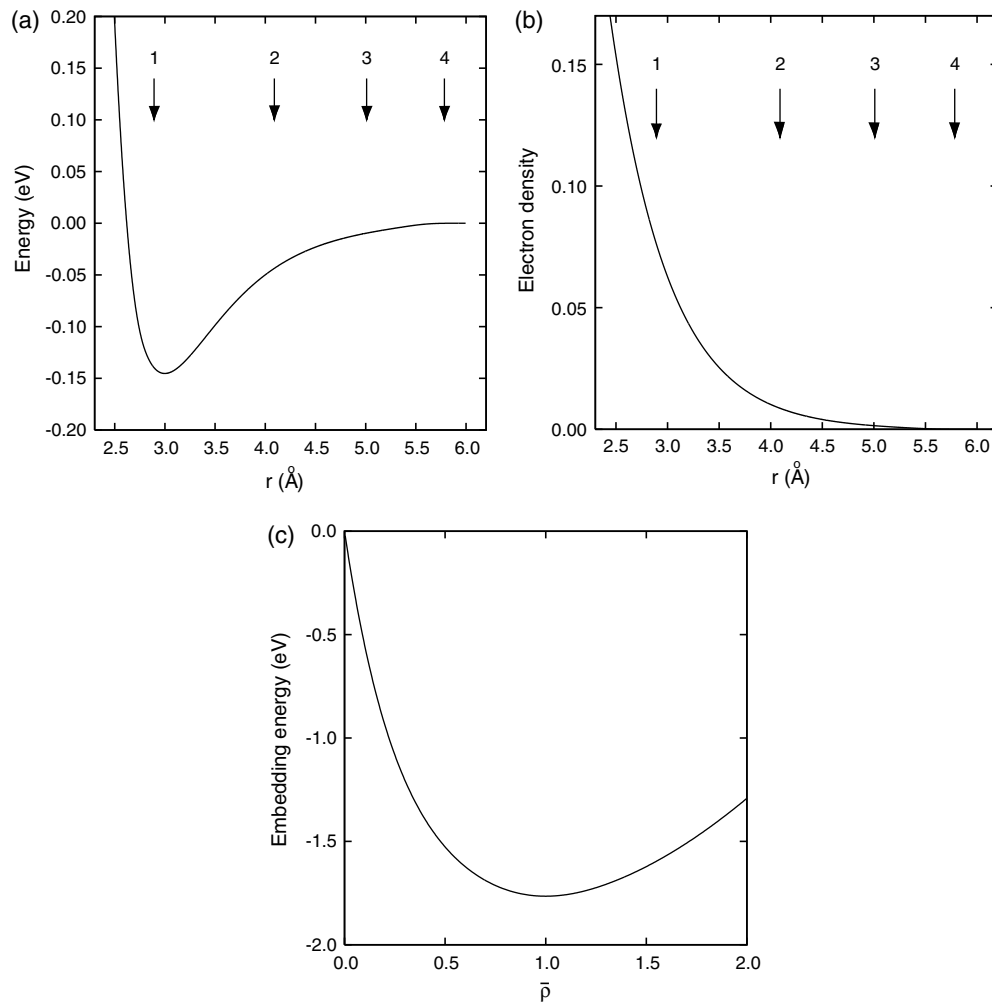


Figure 1. EAM potential functions for Ag: (a) Pair interaction function, (b) electron density function and (c) embedding function. The arrows indicate coordination radii in the equilibrium FCC lattice.

trend of EAM potentials. Attempts to include surface energies in the fitting process and enforce higher values resulted in a poorer fit to structural energies.

The equilibrium structural energies relative to the FCC structure (table 5) compare with first-principles calculations fairly well. Note that it is the whole energy-volume curves (figure 4) that were used in the fit but not the equilibrium energies.

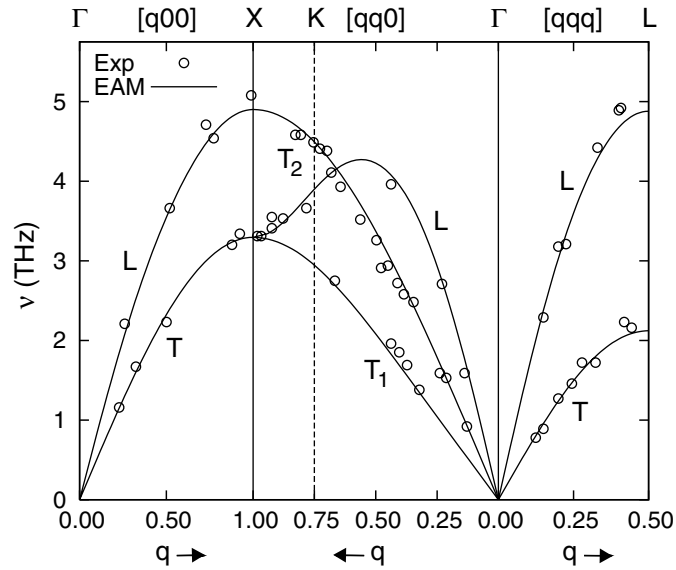
2.3. Binary potential Cu–Ag

Having the elemental potentials for Cu and Ag, the cross-potential $V_{\text{CuAg}}(r)$ has been generated. It is represented by a generalized Morse function

$$V_{\text{CuAg}}(r) = E_1[\exp(-\alpha\beta(r - r_0)) - \alpha \exp(-\beta(r - r_0)) + \delta]\psi\left(\frac{r - r_c}{h}\right) \quad (9)$$

Table 2. Lattice properties of Ag calculated with the EAM potential in comparison with experimental data.

Property	Experiment	EAM
a_0 (Å) ^a	4.09 ^b	4.09
E_0 (eV atom ⁻¹) ^a	-2.85 ^c	-2.85
<i>Elastic constants (GPa)^a</i>		
B	140 ^d	140
c_{11}	124 ^d	124.2
c_{12}	93.4 ^d	93.9
c_{44}	46.1 ^d	46.4
<i>Phonon frequencies (THz)</i>		
$L(X)$ ^a	5.08 ^e	4.90
$T(X)$ ^a	3.34 ^e	3.29
$L(L)$	4.92 ^e	4.88
$T(L)$	2.23 ^e	2.12
$L(K)$	3.70 ^e	3.90
$T_1(K)$	3.04 ^e	2.94
$T_2(K)$	4.49 ^e	4.49

^a Included in the fitting database.^b [20]; ^c [24]; ^d [21]; ^e [25].**Figure 2.** Phonon dispersion curves in Ag calculated with the EAM potential and compared with experimental data (circles, [25]).

with parameters E_1 , r_0 , α , β , δ , r_c and h . The scaling factor of the electron density of Ag, s_{Ag} , and the transformation coefficients g_{Cu} and g_{Ag} [2, 17, 18] were also used as fitting parameters.

The fitting database was generated by VASP calculations similar to those performed for pure Ag. It includes energy-volume relations for seven intermetallic compounds: $L1_2$ -Cu₃Ag, $D0_{22}$ -Cu₃Ag, $L1_0$ -CuAg, $B1$ -CuAg, $B2$ -CuAg, $L1_2$ -CuAg₃ and $D0_{22}$ -CuAg₃. These

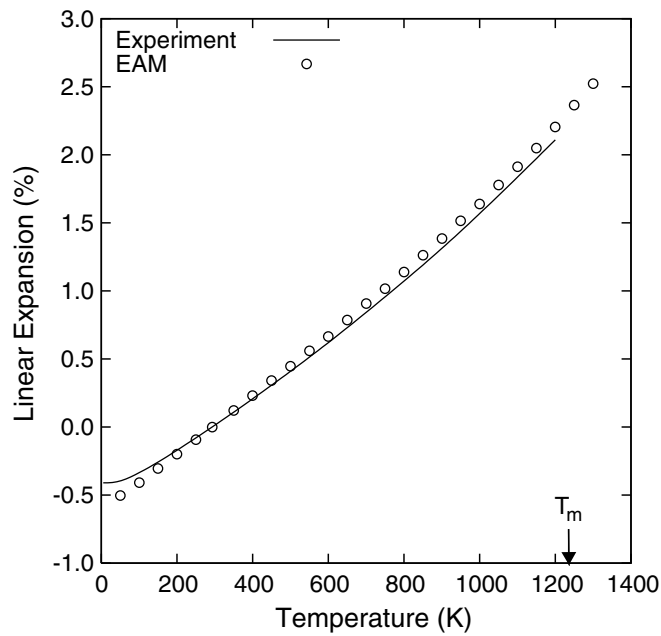


Figure 3. Linear thermal expansion of Ag relative to room temperature calculated by the NPT Monte Carlo method using the EAM potential and compared with experimental data ([28]). The arrow marks the experimental melting point T_m .

Table 3. Lattice defect properties of Ag calculated with the EAM potential in comparison with experimental data and first-principles calculations. Notations: E_v^f , vacancy formation energy; Ω_v , vacancy formation volume; Ω_0 , equilibrium atomic volume; E_v^m , vacancy migration energy; E_i^f , interstitial formation energy for a $\langle 100 \rangle$ -oriented split dumbbell; Ω_i , interstitial formation volume; E_i^m , interstitial migration energy; γ_{SF} , intrinsic stacking fault energy; γ_{us} , unstable stacking fault energy; γ_T , symmetrical twin boundary energy and γ_s , surface energy.

Property	Experiment	<i>ab initio</i>	EAM
<i>Vacancy</i>			
E_v^f (eV) ^a	1.1 ^b	1.06 ^c , 1.20 ^d	1.103
Ω_v/Ω_0	0.94 ^e		0.684
E_v^m (eV) ^a	0.66 ^b		0.655
<i>Interstitial</i>			
E_i^f (eV)			3.226
Ω_i/Ω_0			1.254
E_i^m (eV)	0.088 ^f		0.076
<i>Planar faults (mJ m⁻²)</i>			
γ_{SF} ^a	16 ^g	21 ^h , 33 ⁱ , 46 ^j , 50 ^k	17.8
γ_{us}		190 ^k	115
γ_T	8 ^g	14 ^h , 19 ⁱ	9.2
<i>Surfaces (mJ m⁻²)</i>			
$\gamma_s(110)$	1140 ^l	1260 ^m , 1400 ⁿ	1017
$\gamma_s(100)$	1140 ^l	1210 ^m , 1300 ⁿ	940
$\gamma_s(111)$	1140 ^l	1210 ^{c,m}	862

^a Included in the fitting database.

^b [42]; ^c [43]; ^d [44]; ^e [45]; ^f [46]; ^g [47]; ^h [48] (unrelaxed energy); ⁱ [49]; ^j [50]; ^k [29]; ^l For average orientation [47]; ^m [51]; ⁿ [52].

Table 4. Multilayer relaxation for the (100), (110) and (111) surfaces of Ag calculated with the EAM potential in comparison with first-principles calculations and experimental data. The results are given as the change (in %) from the bulk value of the spacing. The negative and positive values indicate the contraction and expansion, respectively.

	Δd_{12}	Δd_{23}	Δd_{34}	Δd_{45}	
(111)	−1.76	−0.03	0.01	0.00	EAM
	−1.4				<i>ab initio</i> ^a
	−2.5 ~ 10				Experiment ^b
(100)	−2.22	−0.38	0.03	0.00	EAM
	−1.9				<i>ab initio</i> ^a
	0.0 ± 1.5				Experiment ^c
(110)	−6.27	0.48	−0.79	0.31	EAM
	−3.6				<i>ab initio</i> ^a
	−7.8 ± 2.5	4.3 ± 2.5			Experiment ^d

^a [51]; ^b [53]; ^c [54]; ^d [55].

Table 5. Equilibrium energies (in eV) of alternative structures of Ag obtained with the EAM potential in comparison with first-principles calculations.

Structure	<i>ab initio</i>	EAM
HCP	0.003	0.004
BCC	0.039	0.033
SC	0.428	0.400
DC	1.054	0.967

Note: The energies are given relative to the equilibrium FCC structure.

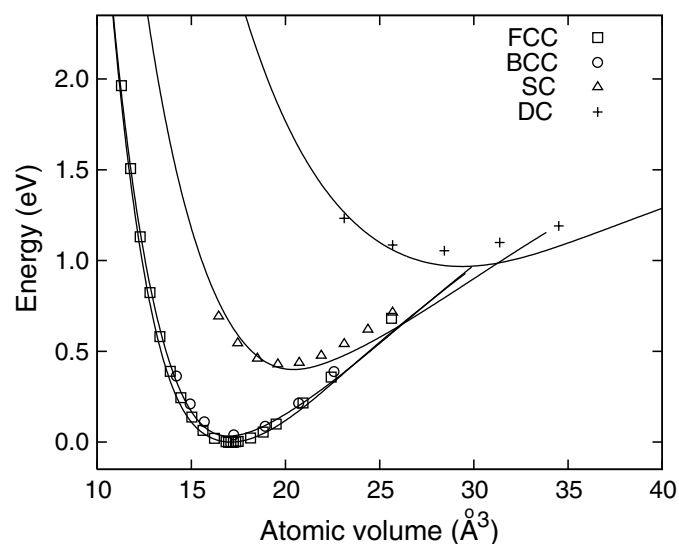
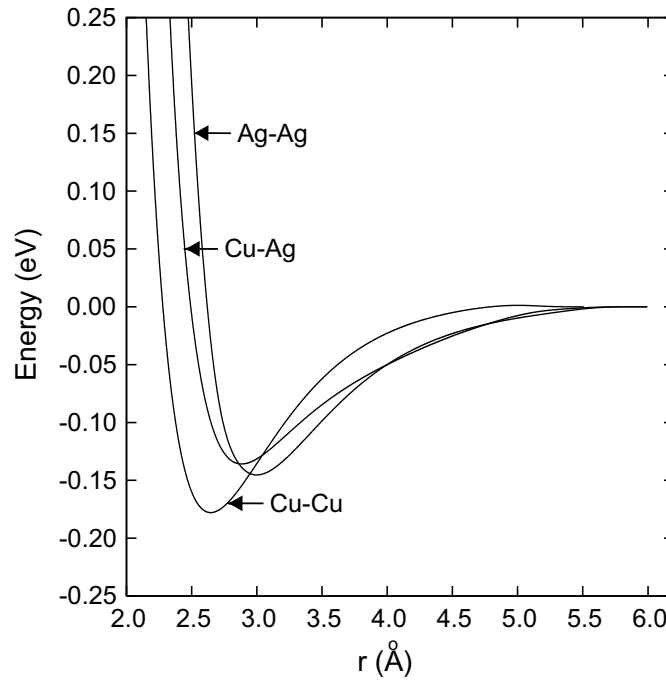


Figure 4. Comparison of *ab initio* (points) and EAM calculated (curves) equations of state of the FCC, BCC, SC and DC structures of Ag relative to the equilibrium FCC structure.

compounds do not exist on the experimental phase diagram [8] and only serve to sample various FCC and BCC-type atomic environments with three different stoichiometries across the entire composition range. Each function $E(\Omega)$ contained 7 points around the equilibrium volume. Prior to the fitting process, all interatomic distances were scaled by the factor S used

Table 6. Optimized values of fitting parameters of the EAM cross-potential Cu–Ag.

Parameter	Value	Parameter	Value
r_c (Å)	5.2	β (Å ⁻¹)	0.349 06
h (Å)	4.533	δ	116.405 1
E_1 (eV)	6.36726×10^{-2}	s_{Ag}	0.694 12
r_0 (Å)	4.435 91	g_{Cu}	-4.978 94
α	6.670 54	g_{Ag}	-10.504 58

**Figure 5.** Pair interaction functions of the EAM potential for the Cu–Ag system in the effective pair format.

previously for pure Ag. The usage of the same scaling factor for pure Ag and the compounds is justified by the fact that scaling factors for Ag and Cu are very close.

The fitting was implemented by minimizing the mean-squared deviation between the EAM and first-principles formation energies of the seven compounds at all atomic volumes. The formation energy of a compound Cu_mAg_n is defined as

$$E(\Omega) - \frac{m}{m+n} E_0^{\text{Cu}} - \frac{n}{m+n} E_0^{\text{Ag}}, \quad (10)$$

where E_0^{Cu} and E_0^{Ag} are the equilibrium cohesive energies of FCC Cu and Ag, respectively, and $E(\Omega)$ is the energy of the compound per atom. We emphasize that no experimental data were used in this fit.

Table 6 contains the optimized values of the fitting parameters. Figure 5 displays the pair potential functions Cu–Cu, Cu–Ag and Ag–Ag transformed to the binary effective pair format [2, 17].

Table 7. Formation energies (in eV) of alternate structures of CuAg, Cu₃Ag and Ag₃Cu compounds obtained with the EAM potential in comparison with first-principles calculations.

Cu ₃ Ag			CuAg			Ag ₃ Cu		
Structure	<i>ab initio</i>	EAM	Structure	<i>ab initio</i>	EAM	Structure	<i>ab initio</i>	EAM
L1 ₂	0.093	0.096	L1 ₀	0.118	0.118	L1 ₂	0.082	0.083
D0 ₂₂	0.095	0.110	B2	0.128	0.177	D0 ₂₂	0.083	0.088
			B1	0.518	0.516			

Table 8. Impurity solubility energies (E_s) and volumes (Ω_s , normalized by the atomic volume Ω_0 of the matrix) of Ag in Cu and Cu in Ag calculated with the EAM potential in comparison with experimental data [9] measured at 1052 K.

Property	Ag in Cu		Cu in Ag	
	Experiment	EAM	Experiment	EAM
E_s (eV)	0.39	0.389	0.25	0.310
Ω_s / Ω_0		0.533		−0.294

2.4. Testing of the Cu–Ag potential

Table 7 presents the equilibrium formation energies of CuAg, Cu₃Ag and Ag₃Cu compounds used in the fit. The agreement with the target values is reasonable. Note that the D0₂₂ structures compete with the L1₂ structures for stability and have only slightly higher energies.

Impurity solubility energies and volumes at $T = 0$ K were computed using a 864-atom cubic supercell. A single point defect was created in the centre of the supercell and the total energy was minimized with respect to local atomic displacements and the supercell volume. The solubility energies predicted by the potential compare favourably with experimental values derived from the heats of solution measured at the experimental eutectic temperature [9] (table 8). The large values and opposite signs of the solubility volumes reflect the large atomic size misfit between Cu and Ag.

3. Thermodynamic calculations

To test the ability of the EAM potential for predicting high temperature properties, the equilibrium lines on the Cu–Ag phase diagram have been calculated. The calculation procedure is similar to the one used previously for the Ni–Al system [7].

The first step of the calculation was to obtain the Gibbs free energies, $g(T)$, of pure Cu and Ag. The NPT Monte Carlo simulations that were used for the calculation of thermal expansion factors in section 2.2 also provided the average potential energy of the crystal per atom, $\varepsilon(T)$, at each temperature T . The total internal energy per atom, $\varepsilon_{\text{tot}}(T)$, was obtained by adding to $\varepsilon(T)$ the classical kinetic energy $3k_B T/2$, k_B being the Boltzmann factor. Because $p = 0$ was enforced, $\varepsilon_{\text{tot}}(T)$ can be equated to the enthalpy $h(T)$. Each $h(T)$ curve was approximated by a quadratic function

$$h(T) = h_0 + AT + BT^2, \quad (11)$$

with fitting parameters h_0 , A and B . The Gibbs free energy was then determined by integrating the Gibbs equation [31] between a reference temperature T^0 and a temperature $T > T^0$:

$$g(T) = g^0 \frac{T}{T^0} + h_0 \left(1 - \frac{T}{T^0}\right) - BT(T - T^0) - AT \ln \left(\frac{T}{T^0}\right). \quad (12)$$

Table 9. Thermodynamic parameters describing FCC Cu and Ag (see section 3 for details).

	g^0 (eV)	h_0 (eV)	$A(10^{-3}/K)$	$B(10^{-6}/K^2)$
Cu	-3.5597	-3.5385	0.247 44	0.024 044
Ag	-2.9043	-2.8477	0.235 94	0.030 949

Note: The reference temperature is $T^0 = 293$ K.

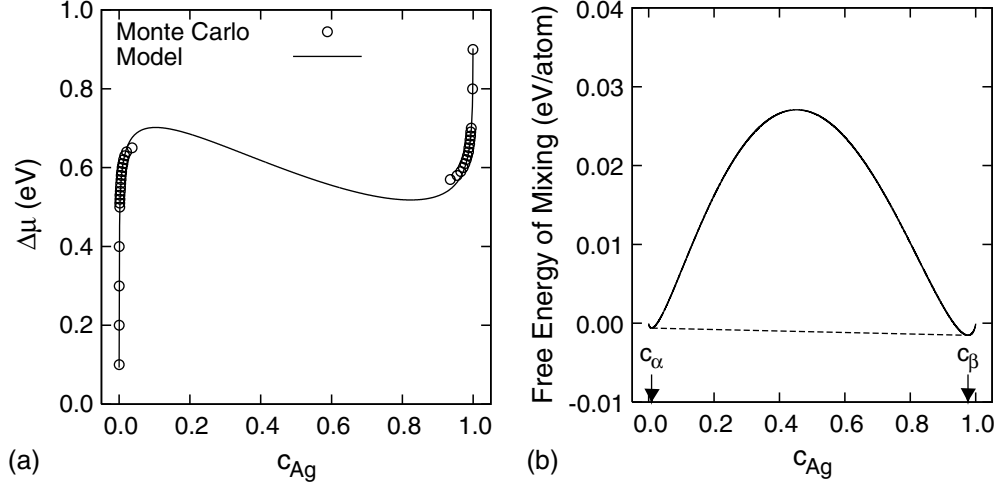


Figure 6. Thermodynamic functions of Cu–Ag alloys at 800 K: (a) Chemical potential difference and (b) Gibbs free energy of mixing (the excess free energy relative to the pure components). The lines were calculated with the thermodynamic model described in the text. (b) shows the common tangent used to compute the solvus concentrations c_α and c_β .

The absolute value of the reference free energy g^0 at $T = T^0$ was obtained using the classical quasi-harmonic approximation [32]. The reference temperature $T^0 = 293$ K was chosen for both Cu and Ag. The thermodynamic parameters obtained are listed in table 9.

The next step of the calculation employed restricted grand-canonical zero-stress Monte Carlo simulations, in which the total number of atoms in a simulation block and the chemical potential difference, $\Delta\mu = \mu_{\text{Ag}} - \mu_{\text{Cu}}$, are fixed while the atom chemical sorts are allowed to switch randomly between Cu and Ag. In addition, individual atoms are subject to random displacements and all three dimensions of the simulation block are allowed to fluctuate independently to ensure a zero-stress condition in each direction. For the solvus line calculations, the simulations employed a 864-atom cubic supercell. For each temperature and $\Delta\mu$, the system was equilibrated by 2×10^3 Monte Carlo steps per atom followed by a calculation of its equilibrium chemical composition averaged over 3×10^4 steps per atom. Each run was repeated for two different initial states of the system: either pure Cu or pure Ag. A plot of the equilibrium alloy composition c_{Ag} (atomic fraction of Ag) against $\Delta\mu$ for a fixed T enables the construction of an isothermal section of the phase diagram, with continuous segments of the plot representing single-phase fields and concentration jumps corresponding to two-phase regions [7, 32]. Our simulations, however, reveal that the α/β transformation is accompanied by a considerable hysteresis (see example in figure 6). Because of this hysteresis, a c_{Ag} versus $\Delta\mu$ plot alone does not allow the α/β equilibrium compositions on the phase diagram to be determined accurately.

To address this problem, the $\Delta\mu(c_{\text{Ag}}, T)$ functions of both phases were approximated by an analytical expression based on a simple thermodynamics model. The model allows us to determine the free energy functions of the phases and thus to locate the phase boundaries by a common tangent construction. The alloy Gibbs free energy, $g(c_{\text{Ag}}, T)$ per atom, is expressed by

$$g(c_{\text{Ag}}, T) = g_{\text{Ag}}(T)c_{\text{Ag}} + g_{\text{Cu}}(T)(1 - c_{\text{Ag}}) + ac_{\text{Ag}} + \frac{b}{2}c_{\text{Ag}}^2 + \frac{c}{3}c_{\text{Ag}}^3 + k_B T [c_{\text{Ag}} \ln(c_{\text{Ag}}) + (1 - c_{\text{Ag}}) \ln(1 - c_{\text{Ag}})], \quad (13)$$

where $a = -b/2 - c/3$. Here $g_{\text{Cu}}(T)$ and $g_{\text{Ag}}(T)$ are the free energies of pure Cu and Ag calculated previously, see equation (12) and table 9. From equation (13) we obtain

$$\Delta\mu(c_{\text{Ag}}, T) = -\frac{\partial g(c_{\text{Ag}}, T)}{\partial c_{\text{Ag}}} = g_{\text{Cu}}(T) - g_{\text{Ag}}(T) - a - bc_{\text{Ag}} - cc_{\text{Ag}}^2 - k_B \ln\left(\frac{c_{\text{Ag}}}{1 - c_{\text{Ag}}}\right). \quad (14)$$

This expression for $\Delta\mu(c_{\text{Ag}}, T)$ was fit to both branches of the Monte Carlo $\Delta\mu(c_{\text{Ag}})$ curve at a fixed temperature by adjusting the parameters b and c (figure 6(a)). With these parameters known, equation (13) gives the free energy curve $g(c_{\text{Ag}})$ at the chosen temperature T . The equilibrium phase concentrations (points on the solvus lines) are then calculated by the common tangent construction implemented numerically (figure 6(b)).

For solidus and liquidus line calculations, restricted grand-canonical zero-stress Monte Carlo simulations were conducted using a 3920-atom supercell containing a solid–liquid interface with the (100) orientation. An alternative approach would be to model the alloy crystallization and melting by molecular dynamics (see, e.g. [6]). In this case, however, slow diffusion processes could give rise to inhomogeneous chemical compositions in the phases. Indeed, the equilibrium phase compositions vary in the course of the crystallization/melting. Limited simulation times may prevent the compositional changes to occur homogeneously since the diffusion processes in the solid phase require the generation, migration and annihilation of vacancies. Monte Carlo simulations were chosen here to circumvent the slow diffusion problem of molecular dynamics (in Monte Carlo all compositional changes occur homogeneously) and to employ a common approach throughout this work.

The direction of the interface motion was monitored as the chemical potential difference $\Delta\mu$ was varied in small increments at a fixed temperature. For each chosen $\Delta\mu$ value, 8.5×10^4 Monte Carlo steps per atom were made to determine $\Delta\mu$ corresponding to the equilibrium condition (no interface motion) within ± 0.005 eV per atom. Then, for each selected temperature and its estimated equilibrium $\Delta\mu$ value, the single-phase compositions were determined by equilibrating the system by 2×10^3 Monte Carlo steps per atom followed by a calculation of its equilibrium chemical composition averaged over 4×10^3 steps per atom. These simulations used the same 3920-atom supercell but started as pure Cu for the α solidus line, pure Ag for the β solidus line and as a homogeneous liquid Cu–Ag alloy for the liquidus lines.

The Cu–Ag phase diagram shown in figure 7 compares the Monte Carlo calculation results with experimental data [8, 9]. All features of the experimental diagram have been reproduced correctly. The estimated eutectic temperature T_E (935 K), eutectic concentration (0.458) and solubility limits (0.03 and 0.937) agree satisfactorily with the experimental values (1053 K, 0.601, 0.049, 0.860, respectively). The melting temperatures of the elements, 1327 K for Cu [33] and 1267 K for Ag, are within 30 K of the experimental values (1358 K for Cu and 1235 K for Ag [20]). The heats of melting of the elements, $H_m = 12.01$ kJ mole^{−1} for Cu and 12.45 kJ mole^{−1} for Ag, calculated in this work compare reasonably well with the experimental values $H_m = 13.03$ kJ mole^{−1} for Cu and 11.30 kJ mole^{−1} for Ag [34].

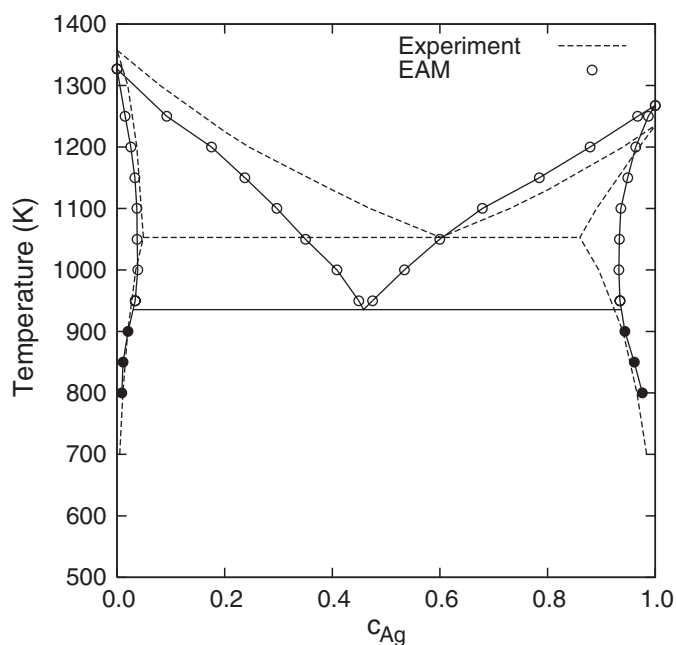


Figure 7. Calculated and experimental [8,9] phase diagram of the Cu–Ag system. Filled circles represent calculations using a thermodynamic model; open circles were obtained from the solid–melt interface simulations.

Although the calculations involving the solid–liquid interface were performed for a particular (100) orientation, we believe that other orientations would give similar results. As indirect evidence, both the melting point and heat of melting of Cu computed for the (100), (110) and (111) interface orientations [33] were found to be almost identical.

As another stringent test, the enthalpy of mixing of liquid Cu–Ag solutions at 1423 K has been calculated by the Monte Carlo method. The liquid composition was varied by adjusting the $\Delta\mu$ value. The energy of a 3920-atom supercell containing an equilibrium liquid solution was averaged over 4×10^3 Monte Carlo steps per atom at zero pressure. The required reference energies of the elemental liquids were determined by similar calculations. The mixing enthalpies predicted by the EAM potential (figure 8) underestimate the values reported by Hultgren and Desai [9] and Hayes *et al* [35]. Although the relative magnitude of the discrepancy is large, it should be noted that the enthalpy of mixing in this system is rather small. The maximum absolute value of the discrepancy, $0.02 \text{ eV atom}^{-1}$, is probably close to the limit of accuracy of this potential. This number is comparable to the mismatch between the EAM and first-principles calculations for structural energies of some of the solid phases, see for example tables 5 and 7.

4. Discussion and conclusions

The EAM Ag potential developed in this work demonstrates very good agreement with both fitted and predicted properties, including elastic constants, phonon frequencies, thermal expansion, lattice-defect energies and energies of alternate structures. Given that the potential generation procedure was similar to the one used previously for Cu [19], both potentials are expected to be nearly equally accurate. Except for experimental thermal expansion factors

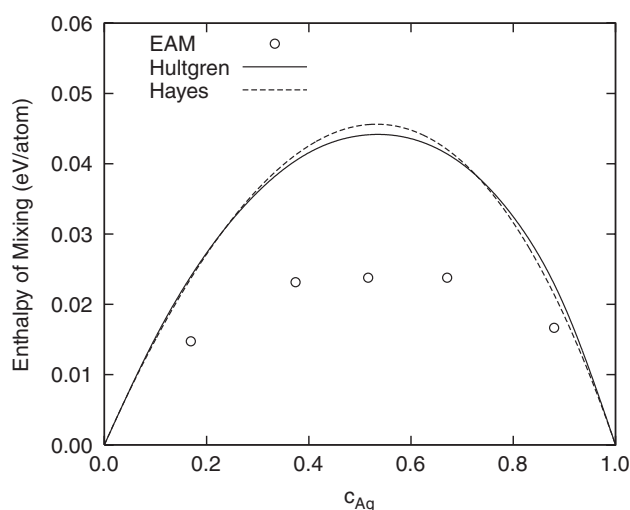


Figure 8. Enthalpy of mixing of liquid Cu–Ag solutions as a function of composition at 1423 K calculated with the EAM potentials and compared with experimental data of Hultgren and Desai [9] and Hayes [35].

used in the potential construction with a small weight, both Cu and Ag potentials are fit to 0 K properties. Although no liquid properties were included in the fitting database, both potentials predict the melting temperatures and heats of melting in reasonable agreement with experiment. This attests to their good transferability to high temperatures.

Although the Cu–Ag cross-interaction function is only fit to first-principles data at 0 K, the calculated Cu–Ag phase diagram is in satisfactory quantitative agreement with experiment. Note that the liquidus/solidus and solvus lines were obtained by two different and independent calculation methods (solid–liquid interface equilibrium above T_E and a thermodynamic model for the free energy below T_E). The apparently smooth junction between the lines obtained by the two methods (figure 7) suggests that the simulation methodology applied in this work is reliable. A conclusion which we draw from figure 7 is that an EAM potential fit accurately to experimental and first-principles data at 0 K can be transferable to high temperatures and can predict a simple binary phase diagram in reasonable agreement with experiment.

This agreement might be further improved by including in the fitting database a set of first-principles energies and/or forces representing liquid configurations. This might raise T_E and shift the eutectic composition towards Ag in better agreement with experiment. This improvement, however, might come at the expense of low-temperature properties. This scheme can be tested in future work.

Even as it is, the new potential set developed in this paper can be useful for atomistic simulations of the Cu–Ag system. For example, we are currently studying Ag segregation at Cu grain boundaries at $T > T_E$ where we expect to see the formation of a thin boundary layer of liquid as we approach the solubility limit. While Ag grain boundary segregation in Cu has been studied by atomistic modelling before [11, 36–38], the possibility of grain-boundary wetting transition has not been examined so far. As another area of applications, it is known experimentally that in 5–10 nm size particles the eutectic temperature is drastically reduced, in some systems even below the liquid–glass transition temperature [39–41]. The Cu–Ag eutectic system can offer a meaningful model for a detailed study of atomistic mechanisms of phase transformations in nanometre-scale particles.

Acknowledgment

This work was supported by the US Department of Energy (Office of Basic Energy Sciences, Division of Materials Sciences) under contract DE-FG02-01ER45871-0006.

References

- [1] Daw M S and Baskes M I 1984 *Phys. Rev. B* **29** 6443
- [2] Mishin Y 2005 *Handbook of Materials Modeling* ed S Yip (The Netherlands: Springer) pp 459–78 chapter 2
- [3] Landa A, Wynblatt P, Siegel D J, Adams J B, Mryasov O N and Liu X Y 2000 *Acta Mater.* **48** 1753
- [4] Hoyt J J, Garvin J W, Webb E B and Asta M 2003 *Modelling Simul. Mater. Sci. Eng.* **11** 287
- [5] Lopasso E M, Carro M, Carro A and Turchi P E 2003 *Phys. Rev. B* **68** 214205
- [6] Baskes M I and Stan M 2003 *Metall. Mater. Trans. A* **34** 435
- [7] Mishin Y 2004 *Acta Mater.* **52** 1451
- [8] Massalski T B (ed) 1986 *Binary Alloy Phase Diagrams* (Materials Park, OH: ASM)
- [9] Hultgren R and Desai P D (ed) 1971 *Selected Thermodynamic Values and Phase Diagrams for Copper and some of its Binary Alloys* (New York: The International Copper Research Association)
- [10] Foiles S M, Baskes M I and Daw M S 1986 *Phys. Rev. B* **33** 7983
- [11] Menyhard M, Yan M and Vitek V 1994 *Acta Metall. Mater.* **42** 2783
- [12] Cai J and Ye Y Y 1996 *Phys. Rev. B* **54** 8398
- [13] Webb E B, Grest G S, Heine D R and Hoyt J J 2005 *Acta Mater.* **53** 3163
- [14] Asta M and Foiles S M 1996 *Phys. Rev. B* **53** 2389
- [15] Najafabadi R, Srolovitz D J, Ma E and Atzmon M 1993 *J. Appl. Phys.* **74** 3144
- [16] Daw M S 1989 *Atomistic Simulation of Materials: Beyond Pair Potentials* ed V Vitek and D J Srolovitz (New York: Plenum) pp 181–91
- [17] Johnson R A 1989 *Phys. Rev. B* **39** 12554
- [18] Voter A F 1994 *Intermetallic Compounds* vol 1 (New York: Wiley) p 77 chapter 4
- [19] Mishin Y, Mehl M J, Papaconstantopoulos D A, Voter A F and Kress J D 2001 *Phys. Rev. B* **63** 224106
- [20] Kittel C 1986 *Introduction to Solid State Physics* (New York: Wiley-Interscience)
- [21] Simmons G and Wang H 1977 *Single Crystal Elastic Constants and Calculated Aggregate Properties* (Cambridge, MA: MIT Press)
- [22] Rose J H, Smith J R, Guinea F and Ferrante J 1984 *Phys. Rev. B* **29** 2963
- [23] Kresse G and Furthmüller J 1996 *Phys. Rev. B* **54** 11169
- [24] Smith C J (ed) 1976 *Metal Reference Book* 5th edn (London: Butterworth)
- [25] 1981 *Metals: Phonon States, Electron States, and Fermi Surfaces (Landolt-Bornstein, New Series, Group III vol 13)* (Berlin: Springer) (Part a)
- [26] Foiles S M 1985 *Phys. Rev. B* **32** 7685
- [27] Frenkel D and Smit B 2002 *Understanding Molecular Simulation* (San Diego: Academic)
- [28] Touloukian Y S, Kirby R K, Taylor R E and Desai P D (ed) 1975 *Thermal Expansion: Metallic Elements and Alloys* vol 12 (New York: Plenum)
- [29] Kioussis N, Herbranson M, Collins E and Eberhart M E 2002 *Phys. Rev. Lett.* **88** 125501
- [30] Bernstein N and Tadmor E B 2004 *Phys. Rev. B* **69** 094116
- [31] Guggenheim E A 1993 *Thermodynamics. An Advanced Treatment for Chemists and Physicists* 4th edn (North Holland: Elsevier)
- [32] Foiles S M 1994 *Phys. Rev. B* **49** 14930
- [33] Suzuki A and Mishin Y 2005 *J. Mater. Sci.* **40** 3155
- [34] Weast R C (ed) 1970 *Handbook of Chemistry and Physics* (Boca Raton, FL: CRC Press)
- [35] Hayes F H, Lukas H L, Effenberg G and Petzow G 1986 *Z. Metallk.* **77** 749
- [36] Creuze J, Berthier F, Tetot R and Legrand B 2000 *Phys. Rev. B* **62** 2813
- [37] Creuze J, Berthier F, Tetot R and Legrand B 2001 *Phys. Rev. Lett.* **86** 5735
- [38] Berthier F, Creuze J, Tetot R and Legrand B 2001 *Appl. Surf. Sci.* **177** 243
- [39] Lee J G, Mori H and Yasuda H 2002 *Phys. Rev. B* **65** 132106
- [40] Lee J G, Mori H and Yasuda H 2002 *Phys. Rev. B* **66** 012105
- [41] Lee J G and Mori H 2004 *Phys. Rev. Lett.* **93** 235501
- [42] Balluffi R W 1978 *J. Nucl. Mater.* **69–70** 240
- [43] Polatoglou H M, Methfessel M and Scheffler M 1993 *Phys. Rev. B* **48** 1877
- [44] Dederichs P H, Hoshino T, Drittler B, Abraham K and Zeller R 1991 *Physica B* **172** 203

- [45] Ehrhart P 1970 *Vacancies and Interstitials in Metals* ed A Seeger *et al* (Amsterdam: North Holland) p 363
- [46] Rizk R, Vajda P, Maury F, Lucasson A and Lucasson P 1977 *J. Appl. Phys.* **48** 481
- [47] Hirth J P and Lothe J 1982 *Theory of Dislocations* 2nd edn (New York: Wiley)
- [48] Hartford J, von Sydow B, Wahnstrom G and Lundqvist B I 1998 *Phys. Rev. B* **58** 2487
- [49] Crampin S, Hampel K, Vvedensky D D and Maclaren J M 1990 *J. Mater. Res.* **5** 2107
- [50] Mehl M J, Papaconstantopoulos D A, Kioussis N and Herbranson M 2000 *Phys. Rev. B* **61** 4894
- [51] Methfessel M, Hennig D and Scheffler M 1992 *Phys. Rev. B* **46** 4816
- [52] Weinert M, Watson R E, Davenport J W and Fernando G W 1989 *Phys. Rev. B* **39** 12585
- [53] Stathis P, Lu H C and Gustafsson T 1994 *Phys. Rev. Lett.* **72** 3574
- [54] Li H, Quinn J, Li Y S, Tian D, Jona F and Marcus P M 1991 *Phys. Rev. B* **43** 7305
- [55] Kuk Y and Feldman L C 1984 *Phys. Rev. B* **30** 5811